Human effector CD8$^+$ T cells with an exhausted-like phenotype control tumor growth *in vivo*

Juliane Mietz[1], Meike Kaulfuss[1], Lukas Egli[1], Lennart Opitz[2], Christian Münz[3], Obinna Chijioke[1,4]

[1]Cellular Immunotherapy, Institute of Experimental Immunology, University of Zürich, Zürich, Switzerland
[2]Functional Genomics Center Zürich, University of Zürich/ETH Zürich, Zürich, Switzerland
[3]Viral Immunobiology, Institute of Experimental Immunology, University of Zürich, Zürich, Switzerland
[4]Institute of Medical Genetics and Pathology, University Hospital Basel, Basel, Switzerland

Corresponding author: Obinna Chijioke, Cellular Immunotherapy, Institute of Experimental Immunology, University of Zürich, Winterthurerstrasse 190, 8057 Zürich, Switzerland; Tel: +41 44 635 37 19, Email: chijioke@immunology.uzh.ch

Abstract

The functional relevance of $CD8^+$ T cell phenotypes in human cancer is not well established. In preclinical studies, murine $CD8^+$ T cells exhibiting an exhausted-like phenotype have been described to have drastically decreased anticancer activity while non-exhausted $TCF\text{-}1^+$ progenitor $CD8^+$ T cells have been thought to be mainly responsible for driving protective antitumor responses. However, human data has mostly been correlative by nature.

By establishing a novel autologous humanized mouse tumor model, we found a $CD8^+$ dominated T cell expansion upon tumor challenge and identified tumor-reactive $CD8^+$ T cells through expression of CD137. This subpopulation of de novo arising human $CD8^+$ T cells displayed a highly proliferative, fully activated effector and exhausted-like phenotype with enhanced expression of exhaustion markers like PD-1, CD39 and TOX, the senescence marker CD57 (*B3GAT1*) and cytolytic effector molecules such as *PRF1*, *GZMH* and *NKG7*. Moreover, these $CD137^+CD8^+$ T cells exhibited tumor-specific clonal expansion and presented signature overlap with tumor-reactive $CD8^+$ T cells described in human cancer. We demonstrate superior anticancer activity of this exhausted-like human $CD8^+$ T cell subset by adoptive transfer experiments using recipients bearing autologous human tumors. Mice adoptively transferred with $CD137^+CD8^+$ T cells showed reduced tumor growth, higher $CD8^+$ T cell persistence as well as tumor infiltration, correlating with control of human tumors.

In summary, we defined effective anticancer activity of human effector $CD8^+$ T cells with an exhausted-like phenotype, supporting clinical exploration of such cells in adoptive T cell therapies.

Keywords: Human cancer immunology; Humanized cancer models; Phenotypic markers; T cells; Exhaustion; Adoptive cell therapy

30 ## Introduction

31 The characterization of phenotypic traits that can faithfully identify tumor-specific $CD8^+$ T cells
32 with functional anticancer activity is an area of intense research. Recent studies have shown
33 tumor-reactive $CD8^+$ T cells to be rare in patients with various cancers and thus challenging to
34 explore[1,2]. While preclinical studies in mice have shown that $CD8^+$ T cells displaying an
35 exhausted-like phenotype have decreased effector function[3], studies in individuals with cancer
36 have correlated exhausted-like phenotypic states of $CD8^+$ T cells with tumor reactivity and
37 clinical benefit[4,5].

38 Undoubtedly, tumor models using inbred and transgenic mice have contributed
39 substantially to our understanding of tumor immunobiology and have been fundamental to the
40 development of cancer immunotherapies that are now used on a routine basis in the clinic[6,7].
41 However, human clinical studies[8] have shown that the outcome of cancer immunotherapies
42 can significantly diverge from those of mouse models of cancer[9]. This might be due to a relative
43 lack of genetic diversity of mouse models compared to humans[10] but also to differences in
44 aspects of gene expression networks[11], genomic organization[12] and tissue structure of the
45 immune system of mice and humans[13]. Xenograft mouse models using adoptive transfer of
46 human immune cells rely on immunodeficient hosts, precluding analysis of the impact of
47 endogenous adaptive antitumor immunity. Furthermore, in most preclinical studies
48 investigating novel immunotherapy targets, monoclonal T cells with a single antigen specificity
49 are explored[14,15] while polyclonal T cell responses might be a biomarker for favorable patient
50 outcome to immunotherapy[16] and thus be more informative.

51 Complementing existing mouse tumor models, the use of mice with reconstituted human
52 immune system components (HIS mice) holds hitherto underexplored translational potential to
53 advance human cancer immunology[17]. Yet, endogenous antitumor immunity in these models
54 has remained largely undefined, mainly due to allogeneic reactivity of the reconstituted human
55 T cells against allogeneic tumors[18], making a distinction of alloreactivity from tumor-specific
56 immune responses challenging.

57 In this study, we demonstrate that reconstitution of human immune system components
58 across independent donors can mount endogenous antitumor T cell responses to autologous

human tumor challenge in HIS mice. A polyclonal population of human effector $CD8^+$ T cells with an exhausted-like phenotype that arises de novo in tumor-bearing HIS mice, resembling exhausted tumor-reactive lymphocytes found in patients with cancer, is able to control autologous human tumor growth *in vivo*. Thus, we provide direct evidence of clinically relevant anticancer activity of expanded human tumor-reactive effector $CD8^+$ T cells with a senescent and exhausted-like, non-progenitor-like phenotype.

88 ## Results

89 **Establishment of an autologous HIS mouse tumor model**

90 We established and characterized a novel tumor model in which immunocompetent,
91 humanized mice are subcutaneously implanted with autologous human tumor cells. For this
92 aim, we isolated $CD34^+$ hematopoietic progenitor cells (HPC) and $CD19^+$ B cells from the same
93 human HPC donor tissue. $CD34^+$ HPCs were engrafted into NSG mice to reconstitute
94 components of the human immune system (from here on referred to as human immune system
95 (HIS) mice), while $CD19^+$ B cells were transformed into lymphoblastoid cell lines (LCL) by
96 infection with the oncogenic Epstein-Barr virus (EBV) (**Figure 1A**).

97 To characterize LCL tumorigenicity and tumor growth in the presence or absence of an
98 autologous human immune system, HIS mice reconstituted with HPCs autologous to the tumor
99 or NSG mice were injected subcutaneously with LCLs. In both recipient strains, palpable
100 tumors formed at the site of implantation. In HIS mice, in the presence of an endogenous
101 immune system, tumors showed progressive growth until approximately day 18 and
102 subsequently, a majority of tumors showed regression (**Figure 1B**). In contrast, in NSG mice
103 without an endogenous immune system, tumors increased in size until termination criteria were
104 reached (**Figure 1C**). These data suggested a functional antitumor response mediated by
105 components of the reconstituted human immune system, i.e. immunocompetence, in our
106 autologous HIS mouse tumor model.

107

108 **Endogenous antitumor immune response in HIS mice**

109 To investigate the tumor regression that we observed in the presence of an autologous human
110 immune system, we next characterized the immune response in tumor-bearing HIS mice.
111 Around the same time of tumor regression, we found weight loss in HIS mice (**Figure 1D**), but
112 not in tumor-bearing NSG mice (**Figure 1E**). This indicated immunopathology related to the
113 endogenous human antitumor immune response, reminiscent of cancer cachexia[19] rather than
114 an effect of tumor growth per se. Additionally, we found increases in spleen-to-body weight
115 ratio, total splenocyte count and white blood cell count in tumor-bearing HIS mice (**Figure 1,**
116 **F-H**), suggesting immune cell proliferation occurring in response to tumor growth. Furthermore,

117 tumors in HIS mice showed infiltration by endogenous human immune cells, including $CD8^+$ T
118 cells (Supplemental Figure 1).

119 The frequency of human $CD3^+$ T cells in tumor-bearing HIS mice in spleen (**Figure 2A**)
120 and circulation (Supplemental Figure 2A) increased significantly compared to naïve HIS mice.
121 Moreover, tumor-bearing HIS mice showed an increased frequency of $CD8^+$ T cells, suggesting
122 preferential expansion (**Figure 2A** and Supplemental Figure 2A). These $CD8^+$ T cells exhibited
123 differentiation towards an effector memory (T_{EM}) phenotype and, to a lower degree, central
124 memory (T_{CM}) phenotype, whereas non-tumor bearing HIS mice had higher frequencies of
125 naïve T cells ($T_{naïve}$) (**Figure 2B** and Supplemental Figure 2B). Consistent with an exhausted
126 effector-like phenotype, $CD8^+$ T cells from tumor-bearing HIS mice also showed enhanced
127 expression of the exhaustion/activation markers PD-1, CD39 and HLA-DR (**Figure 2C** and
128 Supplemental Figure 2C) as well as trending towards increased TOX expression (**Figure 2D**
129 and Supplemental Figure 2D), while exhibiting significantly reduced levels of the
130 progenitor/stemness-related marker TCF-1[20] (**Figure 2D** and Supplemental Figure 2D).

131 Similar to the increased $CD8^+$ T cell frequencies in secondary lymphoid tissue (spleen)
132 and circulation, tumors in HIS mice exhibited predominant infiltration by $CD8^+$ T cells (**Figure**
133 **2E** and Supplemental Figure 1C). The majority of autologous tumor-infiltrating human $CD8^+$ T
134 cells had a T_{EM}-like phenotype, with a lower proportion of T_{CM} and greatly reduced proportions
135 of T_{EMRA} and naïve T cells (**Figure 2F**). Tumor-infiltrating $CD8^+$ T cells displayed high
136 expression of exhaustion and activation markers PD-1 (91.0%±12.1), CD39 (56.4%±22.8) and
137 HLA-DR (53.9%±22.4) (**Figure 2G**), low levels of TCF-1 (5.6%±5.0) (**Figure 2H**), while a
138 fraction of tumor-infiltrating $CD8^+$ T cells expressed TOX (21.7%±14.81) (**Figure 2H**). Together,
139 the phenotype of human $CD8^+$ T cells in tumor-bearing HIS mice was reminiscent of $CD8^+$ T
140 cell phenotypes described in human cancer[21,22].

141

142 **Exhausted, cytotoxic effector-like phenotype of human $CD137^+CD8^+$ T cells**

143 In human cancers, CD137 has been described as a marker for tumor-reactive T cells[23–25]. We
144 similarly identified a population of human $CD137^+$ T cells in tumor-bearing mice (**Figure 2I**)
145 and characterized this $CD8^+$ T cell population further. Likewise, PD-1 has been reported to be

146 a marker of tumor-reactive T cells in human cancers, both in circulation and within tumor-
147 infiltrating lymphocytes[26–28]. We observed that of splenic $CD8^+$ T cells from tumor-bearing HIS
148 mice, only a small proportion (10.9%±11.2) were CD137 positive, whereas the majority of $CD8^+$
149 T cells (83.5%±12.1) expressed PD-1 on their surface (**Figure 2J**). Though there was a small
150 but still significant difference between the overall high level of PD-1 expression on
151 $CD137^+CD8^+$ and $CD137^-CD8^+$ T cells from tumor-bearing HIS mice, both these populations
152 expressed PD-1 significantly more than bulk $CD8^+$ T cells from naïve HIS mice (**Figure 2K**).
153 These data suggested that CD137 alone might not be sufficient to delineate tumor-reactive T
154 cell subsets. We therefore included a $CD8^+$ T cell subset negative for both CD137 and PD-1 in
155 our analysis to further explore and distinguish bona fide tumor-reactive from bystander $CD8^+$
156 T cells in tumor-bearing HIS mice.

157 Indeed, compared to double negative $CD137^-PD\text{-}1^-CD8^+$ T cells, $CD137^+CD8^+$ T cells and
158 $CD137^-CD8^+$ T cells displayed a T_{EM}-like phenotype, while the double negative $CD137^-PD\text{-}1^-$
159 population was enriched in naïve-like T cells (**Figure 2L**). Within the splenic $CD137^+CD8^+$ T
160 cell population, we found the highest expression of the exhaustion marker CD39, which has
161 been described as a marker of $CD8^+$ T cells with enhanced tumor reactivity across different
162 human cancers[1,29–33], the activation marker HLA-DR as well as the activation and residency-
163 related marker CD69[34], while this cell subset also had the strongest expression levels of Ki-
164 67, indicating high proliferation (**Figure 2M**). Additionally, we observed significantly increased
165 expression of TOX, a transcription factor associated with exhaustion[35] and drastically reduced
166 levels of the progenitor/stemness-related transcriptional regulator TCF-1[20] (**Figure 2N**). Finally,
167 $CD137^+CD8^+$ T cells displayed the highest levels of the cytolytic molecules granzyme B and
168 perforin compared with $CD137^-CD8^+$ T cells or $CD137^-PD\text{-}1^-CD8^+$ T cells from tumor-bearing
169 HIS mice (**Figure 2O**). Altogether, de novo arising highly proliferative $CD137^+CD8^+$ T cells
170 exhibited the most exhausted-like, cytotoxic effector and least stem-like phenotype relative to
171 the other human $CD8^+$ T cell populations we identified in tumor-bearing HIS mice.

172

173 **Maintained expansion capacity and enrichment of *in vitro* tumor reactivity within an**
174 **exhausted-like human $CD8^+$ T cell subset**

175 To investigate tumor reactivity of CD137$^+$CD8$^+$ T cells relative to the other T cell subsets,
176 splenic T cells were expanded *ex vivo* (**Figure 3A**). Using a rapid expansion protocol[28], we
177 observed an average expansion of >1000-fold after 14 days for all subsets. Interestingly,
178 although exhausted CD8$^+$ T cells have generally been thought to contain reduced proliferative
179 potential, there were no significant differences in the expansion capacity of CD137$^+$CD8$^+$ T
180 cells displaying the most exhausted-like phenotype (Figure 2, M-N) compared to the other
181 CD8$^+$ T cell populations from tumor-bearing HIS mice or bulk CD8$^+$ T cells from naïve HIS mice
182 (**Figure 3B**). All of the *ex vivo* expanded T cell subsets from tumor-bearing HIS mice exhibited
183 differentiation biased to an effector memory-like phenotype (**Figure 3C**).
184 After co-culture with autologous tumor cells, expanded CD137$^+$CD8$^+$ T cells showed the
185 highest IFN-γ production by ELISpot, which gradually decreased from CD137$^-$CD8$^+$ T cells to
186 CD137$^-$PD-1$^-$CD8$^+$ T cells (**Figure 3D**). Similarly, TNFα secretion was highest in supernatants
187 containing CD137$^+$CD8$^+$ T cells after co-culture with autologous tumor cells and lowest in
188 CD137$^-$PD-1$^-$CD8$^+$ T cells (**Figure 3E**). These data indicated enrichment of tumor recognition
189 within CD137$^+$CD8$^+$ T cells that maintained *ex vivo* proliferative potential, while double negative
190 CD137$^-$PD-1$^-$CD8$^+$ T cells behaved as bystander cells.
191
192 **Transcriptome analysis reveals tumor-reactive signature in CD137$^+$CD8$^+$ T cells**
193 To gain insight into differentially expressed genes (DEG) in tumor-reactive CD137$^+$CD8$^+$ T cells
194 versus CD137$^-$CD8$^+$ T cells and bystander CD137$^-$PD-1$^-$CD8$^+$ T cells as well as bulk CD8$^+$ T
195 cells from naïve HIS mice, whole transcriptome RNA sequencing of *ex vivo* expanded T cell
196 subsets was performed. We found a higher number of DEG for the tumor-reactive (CD137$^+$)
197 gene set versus bystander CD8$^+$ T cells from tumor-bearing HIS mice (200 DEG) and versus
198 bulk CD8$^+$ T cells from naïve HIS mice (300 DEG) in comparison to the number of DEG we
199 found for the comparison against CD137$^-$CD8$^+$ T cells (53 DEG) (**Figure 4A**), the subset with
200 the second highest tumor reactivity *in vitro* (Figure 3, D and E). Principal component analysis
201 (PCA) was consistent with functional data of tumor-specific cytokine production (Figure 3, D
202 and E), showing that the 4 subsets clustered in a gradual way from tumor-reactive (CD137$^+$)
203 to less tumor-reactive (CD137$^-$) and bystander (CD137$^-$PD-1$^-$) CD8$^+$ T cells and finally to bulk

204 CD8$^+$ T cells from naïve HIS mice, with the biggest overlap between CD137$^-$PD-1$^-$ bystander
205 CD8$^+$ T cells and bulk human CD8$^+$ T cells from naïve HIS mice (**Figure 4B**).
206 The transcriptomic profile that we found in tumor-reactive CD137$^+$CD8$^+$ T cells suggested
207 an exhausted/activated-like phenotype with increased expression of *TNFRSF9*, *LAG3*,
208 *PDCD1, TIGIT* and *HLA-DPA1/HLA-DQA1* (**Figure 4, C, E and F**). We also observed
209 enhanced expression of effector molecules associated with cytotoxicity (*GZMH, NKG7* and
210 *PRF1*) as well as *IFNG* (**Figure 4, C, E and F**). Expression of the naïve or stem-like genes
211 *CCR7*, *LEF1* and *BACH2* were diminished (**Figure 4, D-F**) while the senescence marker
212 CD57[36] (*B3GAT1*) and the transcription factor *EOMES* showed the highest transcript level in
213 the CD137$^+$ subset (**Figure 4, C and F**). Although EOMES has been shown to be involved in
214 T cell exhaustion, it has also been reported to be commonly co-expressed with effector
215 molecules in effector T cells and to be essential for anticancer T cell function[37,38].
216 Among upregulated Gene Ontology (GO) terms comparing tumor-reactive CD137$^+$CD8$^+$ T
217 cells against the other three populations, we found the terms interferon-gamma mediated
218 signaling (GO:0060333), antigen processing and presentation (GO:0019882), antigen
219 processing and presentation of peptide or polysaccharide antigen via MHC class II
220 (GO:0002504), immune response (GO:0006955) and adaptive immune response
221 (GO:0002250) (**Figure 4G**). Upregulation of these pathways in the CD137$^+$ population
222 indicated stronger T cell activation and response in comparison to the other populations.
223 Next, we compared our transcriptome data to published datasets of different T cell states
224 from individuals with cancers[21,33,39–41]. Strikingly, comparing tumor-reactive CD137$^+$CD8$^+$ T
225 cells to bystander CD137$^-$PD-1$^-$CD8$^+$ T cells or bulk CD8$^+$ T cells from naïve HIS mice, gene
226 sets that have been described to define tumor-reactive T cells in patients with cancer were
227 significantly upregulated ('MANA TIL'[40], 'tumor specific'[41]) (**Figure 4H**). These results
228 suggested that the antitumor T cell response in autologous tumor-bearing HIS mice mirrors
229 relevant aspects of the T cell response in cancer patients, thus further supporting the potential
230 translational value of our model.
231
232 **Correlation of clonal expansion with effector function**

233 As another surrogate for tumor recognition, we analyzed clonality of the CD8$^+$ T cell receptor
234 (TCR) repertoire, anticipating tumor-reactive CD8$^+$ T cells would have higher clonal expansion
235 and thus lower diversity than bystander CD8$^+$ T cells. Indeed, we found the total number of
236 clonotypes tending to be the smallest in the tumor-reactive CD137$^+$ subset, and to gradually
237 increase from the less tumor-reactive CD137$^-$ subset to CD137$^-$PD-1$^-$ bystander CD8$^+$ T cells
238 to bulk CD8$^+$ T cells from naïve HIS mice (**Figure 5A**), following the gradient of tumor
239 recognition we observed by tumor-specific cytokine production *in vitro* (Figure 3, D and E).
240 Likewise, the estimated sample diversity for the tumor-reactive CD137$^+$ subset was lower than
241 for the other populations (**Figure 5B** and Supplemental Figure 3A). In line with this, the CD137$^+$
242 population had a reduced abundance of rare or very small clonotypes (**Figure 5C** and
243 Supplemental Figure 3, B and C). Conversely, tumor-reactive CD137$^+$ CD8$^+$ T cells from tumor-
244 bearing HIS mice demonstrated a significantly higher abundance of hyperexpanded clones
245 (**Figure 5D**) with the 20 biggest clones occupying a significantly larger repertoire space than
246 in the other populations, suggesting polyclonal expansion (Supplemental Figure 3B).

247 To track the overlap of clonotypes between individual experiments (i.e. donor dependency)
248 and populations, we next performed TCR repertoire overlap analysis (**Figure 5E**). We found
249 that the tumor-reactive CD137$^+$ population showed the biggest overlap with the CD137$^-$ subset
250 and only to a minor extend an overlap with CD137$^-$PD-1$^-$ bystander CD8$^+$ T cells or bulk CD8$^+$
251 T cells from naïve HIS mice (**Figure 5, E and G** and Supplemental Figure 3E). Also, analyzing
252 the repertoire of the bulk naïve CD8$^+$ T cell population for each experiment by cross-comparing
253 to each population from each experiment, the overlap with the CD137$^+$ population was
254 significantly less than the overlap with every other population (**Fig. 5F**). These findings
255 suggested that clonotypes arising due to the conditions of expansion were less present in the
256 CD137$^+$ population and that other, presumably tumor-reactive, clonotypes expanded.

257 In addition, we observed that the expansion of individual bona fide tumor-reactive
258 clonotypes was highly donor specific. When comparing the 10 most abundant clonotypes of
259 the CD137$^+$ population per experiment (i.e. per donor), almost no overlap with the CD137$^+$
260 TCR repertoire of any other experiment was detected (**Figure 5G** and Supplemental Figure
261 3D). Finally, to explore an association of clonal expansion with functionality, we correlated the

262 abundance of the top 10 bona fide tumor-reactive clonotypes of the CD137$^+$ population with *in*
263 *vitro* tumor reactivity and found a highly significant correlation of clone size abundance and
264 tumor-specific IFN-γ production by CD8$^+$ T cells (**Figure 5H**). Overall, these data indicated that
265 CD137$^+$CD8$^+$ T cells derived from tumor-bearing HIS mice expanded polyclonally in a human
266 donor- and tumor-specific manner.
267
268 **Human CD8$^+$ T cells with an exhausted-like phenotype reduce tumor growth *in vivo***
269 We next performed adoptive cell transfer (ACT) experiments of *ex vivo* expanded CD8$^+$ T cells
270 in NSG mice previously engrafted with autologous tumors (**Figure 6A**). We initially selected
271 NSG mice as recipients to unambiguously track the transferred T cells and to be able to
272 distinguish their anticancer activity from the endogenous antitumor T cell response in HIS mice.
273 In NSG mice, only ACT with expanded CD137$^+$CD8$^+$ T cells resulted in reduced tumor growth,
274 while transfer of bystander CD8$^+$ T cells from tumor-bearing HIS mice or bulk CD8$^+$ T cells from
275 naïve HIS mice did not (**Figure 6, B and C**).
276 Furthermore, a higher frequency of T cells was found in tumor (**Figure 6, D and E**), spleen
277 (Supplemental Figure 4A) and blood (Supplemental Figure 4B) of tumor-bearing NSG mice
278 receiving CD137$^+$CD8$^+$ T cells compared to recipients transferred with any of the other cell
279 populations. Flow cytometric analysis of tumor-infiltrating lymphocytes (TIL) revealed high
280 CD3$^+$ T cell frequencies (53.65%±21.94) after ACT of expanded CD137$^+$CD8$^+$ T cells, but only
281 11.64%±11.0 after transfer of bystander CD8$^+$ T cells and 7.25%±5.38 after transfer of bulk
282 CD8$^+$ T cells from naïve HIS mice (**Figure 6D**). Likewise, immunohistochemistry of tumors of
283 NSG mice confirmed T cell infiltration selectively after ACT with CD137$^+$CD8$^+$ T cells (**Figure**
284 **6E**). Thus, human exhausted-like CD137$^+$CD8$^+$ T cells exhibited the potential for persistence
285 and robust tumor infiltration.
286 Interestingly, while infusion products mainly contained a mix of T_{EM}-like and T_{EMRA} CD8$^+$ T
287 cells (Figure 3C), almost exclusively T_{EM}-like cells were recovered from TIL (**Figure 6F**), spleen
288 (Supplemental Figure 4C) and blood (Supplemental Figure 4D) of recipient NSG mice. Of note,
289 whereas PD-1 was highly expressed on splenic CD137$^+$CD8$^+$ T cells in tumor-bearing HIS
290 mice (96.49%±3.1) (Figure 2K), PD-1 expression on this population decreased during antigen-

291 independent *ex vivo* expansion (31.81%±31.81) (Supplemental Figure 5A). However, after
292 adoptive transfer of expanded CD137$^+$CD8$^+$ T cells into tumor-bearing NSG mice, PD-1
293 expression among CD8$^+$ T cells in TIL increased again (96.7%±3.65) and was significantly
294 higher compared with CD8$^+$ T cells recovered from TIL of NSG mice transferred with bystander
295 CD8$^+$ T cells or bulk CD8$^+$ T cells (Supplemental Figure 5B). Apart from the superior tumor
296 control, these data further indicated enrichment of tumor reactivity within CD137$^+$CD8$^+$ T cells,
297 with very high PD-1 expression serving as a potential marker for productive tumor recognition,
298 but not loss of effector function. As another index of the anticancer activity of CD137$^+$CD8$^+$ T
299 cells, the degree of tumor infiltration with CD8$^+$ T cells after ACT was inversely correlated with
300 tumor size (**Figure 6G**). Thus, the higher frequency of CD8$^+$ T cells in tumors was likely driven
301 by increased tumor recognition of transferred CD137$^+$CD8$^+$ T cells, and these cells mediated
302 tumor cell killing.

303 Lastly, ACT of tumor-reactive T cells into autologous tumor-bearing HIS recipient mice
304 (**Figure 6H**) presented an opportunity to model polyclonal TIL transfer therapy in cancer
305 patients[42] in an immunocompetent humanized tumor setting. As observed with NSG recipients,
306 transfer of polyclonal tumor-reactive CD137$^+$CD8$^+$ T cells into autologous tumor-bearing HIS
307 recipient mice reduced tumor growth (**Figure 6, I and J**). Importantly, this was achieved without
308 prior conditioning of HIS recipient mice or cytokine support, and the number of transferred
309 tumor-reactive CD137$^+$CD8$^+$ T cells was fivefold lower compared with transfer in NSG
310 recipients. These data established superior anticancer activity of CD137$^+$CD8$^+$ T cells with an
311 exhausted-like phenotype the most complete humanized setting.

312 Altogether, these adoptive transfer experiments confirmed anticancer activity of human
313 CD137$^+$CD8$^+$ T cells that developed in autologous tumor-bearing HIS mice, suggesting that
314 our model captured relevant aspects of the immunobiology of human antitumor T cell
315 responses.

316

317

318

319

320 ## Discussion

321 Using in-depth phenotypic analyses, *in vitro* functional assays and adoptive transfer
322 experiments, we identified a proliferative human $CD8^+$ T cell subset in tumor-bearing HIS mice
323 that expressed senescence and exhaustion markers including very high levels of PD-1 and
324 CD39 while having low expression of the progenitor marker TCF-1 but exhibited increased
325 tumor reactivity. By means of adoptive transfer, we uniquely provide direct *in vivo* evidence of
326 superior anticancer activity of these human tumor-reactive effector $CD8^+$ T cells displaying a
327 senescent and exhausted-like phenotypic state.

328 We have leveraged this human $CD8^+$ T cell subset arising de novo in tumor-bearing HIS
329 mice for transcriptomic analysis and TCR profiling to demonstrate across donors overlap with
330 tumor-reactive $CD8^+$ T cell signatures from human cancers[40,41] as well as tumor-induced
331 polyclonal expansion. Polyclonality of neoantigen-specific $CD8^+$ T cells in blood and tumor has
332 recently been shown to be associated with response to PD-1 immunotherapy in patients with
333 melanoma[16]. Congruence of our model data across donors with these clinical benchmarks
334 suggests robustness and translational validity of our findings.

335 Of note, $CD39^+CD8^+$ T cells expressing high levels of PD-1 have been described to be
336 enriched for tumor reactivity and clonal proliferation, predicting efficacy of immunotherapy in
337 human lung cancer[33]. Likewise, the abundance of intratumoral $CD39^+CD8^+$ T cells displaying
338 upregulated exhaustion markers has been shown to be prognostic for improved progression-
339 free and overall survival in individuals with treatment-naïve early stage lung cancer[43].
340 Furthermore, PD-$1^{hi}CD39^+CD8^+$ T cells correlated with improved survival in patients with
341 endometrial cancer[32] and the signature of similar $CD8^+$ T cells with increased TOX expression
342 predicted survival in patients with breast cancer[31]. Recently, pre-existing exhausted-like tumor-
343 reactive $CD8^+$ T cells have been associated with favorable outcome to immunotherapy in head
344 and neck cancer[44]. On the other hand, higher abundance of TCF-1^+ stem-like $CD8^+$ T cells with
345 a $CD39^-CD69^-$ phenotype in TIL products was associated with better response after TIL
346 transfer in patients with melanoma[45]. However, by single-cell analysis of lung tumors, this
347 phenotype could not be identified in neoantigen-reactive T cells[46]. While we have not
348 addressed and thus cannot exclude a contribution of the minor TCF-1^+ fraction within the

349 human tumor-reactive CD8$^+$ T cells in our model, our data emphasize the key importance of
350 exhausted-like effector CD8$^+$ T cells in the antitumor immune response.

351 The striking phenotypic similarity of tumor-reactive CD8$^+$ T cells that have been shown to
352 correlate with clinical benefit and the polyclonally expanded human tumor-reactive CD8$^+$ T cell
353 cells from tumor-bearing HIS mice that we demonstrated to possess superior *in vivo* anticancer
354 activity highlights the translational potential of our model. Hence, the novel immunocompetent
355 human tumor model that we developed using HIS mice with human immune cells reconstituted
356 from hematopoietic progenitor cells that are autologous to tumor might bridge a gap between
357 syngeneic mouse tumor models and human-specific antitumor immune responses[13,47]. Our
358 model demonstrates hallmarks of human antitumor T cell responses and thus may provide a
359 tool that should allow further investigation of drivers of anticancer activity in human CD8$^+$ T
360 cells. Overall, the endogenous human immune system in HIS mice markedly influenced tumor
361 and host, allowing for experimental interrogation of the interfaces of human tumor and
362 autologous human antitumor immunity in a small animal model.

363 Together, fully activated effector and exhausted-like human CD8$^+$ T cells directly mediate
364 anticancer activity. Our data support clinical exploration of exhausted-like effector CD8$^+$ T cell
365 subsets alongside the recently more favoured stem-like phenotype for use in adoptive transfer
366 and engineered T cell therapies.
367
368
369
370
371
372
373
374
375
376
377

Methods

HIS & NSG mice

NSG (NOD.Cg-Prkdc<scid>Il2rg<tm1Wjl>/SzJ (#005557)) mice were purchased from The Jackson Laboratory and bred and housed under specific pathogen-free conditions at the Laboratory Animal Services Center (LASC) Zurich, University of Zurich. To generate HIS mice, newborn pups (1-5 days old) were irradiated (1 Gy) and intrahepatically injected with 0.2 x 10^6 human $CD34^+$ hematopoietic progenitor cells derived from human fetal liver (Advanced Bioscience Resources, USA). $CD34^+$ cells were isolated by MACS technology (Miltenyi, Cat. 130-046-703) following the manufacturer's instructions. At 3 months of age, reconstitution of human immune cells was assessed in PBMC from tail vein blood by flow cytometry[48]. Reconstitution analysis included staining for human CD45, CD3, CD4, CD8, CD19, NKp46 and HLA-DR. Only mice with a sufficiently high frequency of human CD45 (>25% of leukocytes) were included in the experiments. All animal experiments were performed according to approved licenses by the veterinary office of the canton of Zurich, Switzerland (ZH049/20 and ZH067/2023).

LCL generation and tumor model

LCL were generated from $CD19^+$ B cells derived from the same autologous human fetal liver tissue from which the $CD34^+$ cells for reconstitution of the human immune system in the same experiment were derived. $CD19^+$ cells were isolated from the HFL tissue's $CD34^-$ fraction by MACS technology (Miltenyi, Cat. 130-050-301) according to the manufacturer's instructions. 0.25 x 10^6 $CD19^+$ human B cells were transformed by infection with Epstein-Barr virus (EBV B95-8; produced as previously described[48]) at an MOI of 0.1 - 0.15 and cultured in RPMI/ 10% FCS/ 1% Penicillin/ Streptomycin.

LCL tumors were injected subcutaneously into the left flank under isoflurane narcosis. For generation and phenotyping of tumor-reactive T cells, 5 x 10^6 autologous LCL tumor cells were resuspended in PBS and right before injection mixed in a 1:1 V/V ratio with Corning® Matrigel® Growth Factor Reduced (GFR) Basement Membrane Matrix (Milian, Cat. 354230).

406 For adoptive cell transfer experiments, 2 x 10^6 LCL were injected s.c. in a 1:1 V/V mix with
407 Matrigel and three days after tumor injection, 2 x 10^6 T cells (HIS recipient mice) or 10 x 10^6
408 (NSG recipient mice) were adoptively transferred by tail vein injection. Tumor size was
409 monitored by calipering (3x/week or daily). Tumor volume was calculated as volume [mm^3] =
410 length [mm] x $width^2$ [mm^2] x 0.52. General health was monitored by weighing and health
411 parameter scoring (3x/week or daily, according to animal license). PBMC composition and
412 expansion of adoptively transferred T cells were monitored by weekly tail vein bleeding and
413 flow cytometric analysis. White blood cell (WBC) counts were measured from blood with an
414 automatic cell counting machine (DxH 500, Beckman Coulter). Animals were euthanized when
415 they met pre-defined termination criteria defined in the animal license.
416
417 **T cell isolation and expansion**
418 Spleens from LCL tumor-bearing and naïve HIS mice were harvested 16-18 days after s.c.
419 tumor injection. Splenocytes were labelled with fluorescently labelled antibodies and sorted by
420 fluorescent activated cell sorting (FACS). $CD137^+$, $CD137^-$ and $CD137^-PD\text{-}1^-$ $CD8^+$ T cells were
421 sorted from tumor-bearing HIS mice and bulk $CD8^+$ T cells were isolated from naïve HIS mice.
422 Sorted T cells were expanded by a rapid expansion protocol (REP), as described elsewhere[28].
423 REP medium consisted of a 1:1 mix of RPMI (Gibco, Cat. 7001612) and X-Vivo (Lonza, Cat.
424 BE02-060F) containing 10% FCS (Biochrome, Cat. S0615-500ML) and 1% Penicillin/
425 Streptomycin (Thermo Fisher, Cat. 7001592). After sorting, T cells were cultured in REP
426 medium with 30 ng/µl OKT3 (Miltenyi, Cat. 130-093-387), 3000 IU/ml IL-2 (Peprotech, Cat.
427 200-02) and a 200-fold excess of irradiated (50 Gy) allogeneic PBMC derived from 3 healthy
428 donors at a total cell density of 5 x 10^6 cells/ml. Starting at day 7, cells were adjusted with REP
429 medium to 0.5-1 x 10^6 cells/ml and fresh IL-2 (3000 IU/ml) was added every second day. Cells
430 were expanded for a total of 14-16 days until use for further experiments.
431
432 **Cell isolation from organs**
433 For reconstitution analysis and weekly bleeding, 100-150 µl of tail vein blood was collected
434 into EDTA tubes (BD Microtainer, BD, Cat. 365975) and erythrocytes were lysed by incubation

435 with lysis buffer. Leukocytes were stained for flow cytometric analysis. For PBMC isolation on
436 the day of sacrifice, blood was harvested by heart puncture and erythrocytes were lysed with
437 erythrocyte lysis buffer. For splenocyte isolation, spleens were removed and meshed through
438 a 70 µm cell strainer in PBS and lymphocytes were isolated by Ficoll-Paque (GE Healthcare,
439 17-5442-03). Single cell suspensions were washed and stained for flow cytometric analysis.
440 For tumor-infiltrating lymphocyte (TIL) isolation, tumors were removed from the flank and skin
441 was removed from the tumors. Tumors were cut into small pieces with scissors and then
442 incubated with digestion mix (DMEM (Life technologies, Cat. 7001566) containing 2% FCS
443 (Biochrome, Cat. S0615-500ML), 1 mg/ml Collagenase IV (Roche, Cat. 7002219), 10ug/ml
444 DNase I (Roche, Cat. 7002221) and 1.2 mM CaCl2; approx. 1.5 ml/tumor, incubation for 45
445 min, 37°C). The tumor digest was diluted with 20 ml RPMI or PBS and meshed over a 70 µm
446 cell strainer. Single cell suspensions were washed and then stained for flow cytometric
447 analysis.
448
449 **Flow cytometry**
450 For surface staining, cells were washed in PBS and stained with an antibody master mix for
451 20 min at 4°C in the dark. For intracellular staining, cells were first stained for surface antigens
452 and fixable live/dead marker, then fixed and permeabilized using the BD Pharmingen™
453 Transcription Factor Buffer Set (BD, Cat. 562574) according to the manufacturer's instructions,
454 then stained for intracellular or intranuclear antigens for 50-60 minutes. Cells were washed in
455 PBS and acquired on a BD LSRFortessa™.
456 Antibodies for reconstitution analysis of HIS mice (all antibodies are anti-human): CD45-Pacific
457 Blue (Biolegend, HI30, Cat. 304029), CD3-PE (Biolegend, UCHT1, Cat. 300408), CD4-APC-
458 Cy7 (Biolegend, RPA-T4, Cat. 300518), CD8-PerCP (Biolegend, SK1, Cat. 344708), HLA-DR-
459 FITC (Biolegend, L243, Cat. 307604), CD19-PE-Cy7 (Biolegend, HIB19, Cat. 302216),
460 NKp46-APC (BD, 9-E2, Cat. 558051), Zombie Aqua™ Fixable Viability Kit (Biolegend, Cat.
461 423101).
462 Antibodies for flow cytometry-based sorting of T cells: CD3-FITC (Biolegend, UCHT1, Cat.
463 300406), CD4-APC-Cy7 (Biolegend, RPA-T4, Cat. 300518), CD8-BV650 (Biolegend, SK1,

464 Cat. 344730), CD45-Pacific Blue (Biolegend, HI30, Cat. 304029), CD137-APC (Miltenyi,
465 REA765, Cat. 130-110-901), PD-1-PE-Dazzle (Biolegend, EH12.2H7, Cat. 329940), Zombie
466 Aqua™ Fixable Viability Kit (Biolegend, Cat. 423101).
467 Antibodies for phenotyping in Panel 1: CD45-Pacific Blue (Biolegend, HI30, Cat. 304029),
468 CD3-PerCP-Cy5.5 (Biolegend, UCHT1, Cat. 300429), CD4-APC-Cy7 (Biolegend, RPA-T4,
469 Cat. 300518), CD8-BV650 (Biolegend, SK1, Cat. 344730), CD45RA-BV785 (Biolegend,
470 HI100, 304139), CD62L-FITC (BD, DREG-56, Cat. 555543), CD19-PE-Cy7 (Biolegend,
471 HIB19, Cat. 302216), HLA-DR-BV605 (BD, g46-6, Cat. 562845), CD39-BV711 (Biolegend, A1,
472 Cat. 328228), CD69-Alexa Fluor 700 (Biolegend, FN50, Cat. 310921), PD-1-PE-Dazzle
473 (Biolegend, EH12.2H7, Cat. 329940), TCF-1-PE (Biolegend, 7F11A10, Cat. 655207), CD137-
474 APC (Miltenyi, REA765, Cat. 130-110-901), Zombie Aqua™ Fixable Viability Kit (Biolegend,
475 Cat. 423101); in Panel 2: CD3-FITC (Biolegend, UCHT1, Cat. 300406), CD4-PE-Cy7
476 (Biolegend, RPA-T4, Cat. 300512), CD8-BV650 (Biolegend, SK1, Cat. 344730), CD45-BV711
477 (Biolegend, HI30, Cat. 304050), CD137-APC-Fire750 (Biolegend, 4B4-1, Cat. 309834),
478 Granzyme B-APC-Alexa700 (Biolegend, QA16A02, Cat. 372222), Ki-67-BV605 (Biolegend,
479 Ki-67, Cat. 350522), PD-1-PE-Dazzle (Biolegend, EH12.2H7, Cat. 329940), Perforin – BV421
480 (Biolegend, dG9, Cat. 308122), TCF-1-PE (Biolegend, 7F11A10, Cat. 655207), TOX-APC
481 (Miltenyi, REA473, Cat. 130-118-335), Zombie Aqua™ Fixable Viability Kit (Biolegend, Cat.
482 423101).
483
484 **IFN-γ ELISpot and TNFα ELISA**
485 For IFN-γ ELISpot, ELISpot plates (Merck, Cat.MAIPN4550) were activated with 35% ethanol,
486 washed and coated overnight with anti-IFN-γ coating antibody (mAb-1-D1K, Mabtech, Cat.
487 3420-3-1000). Plates were washed and T cells were co-cultured with autologous LCL in RPMI/
488 10% FCS/ 1% Pen/Strep at an effector: target ratio of 5:1 for 16-24 hours. After incubation,
489 supernatant was harvested, stored at -20°C and used for TNFα ELISA. Wells were washed
490 and incubated for 2 hours with biotinylated anti-IFN-γ detection antibody (mAb-7-B6-1-Biotin,
491 Mabtech, Cat. 3420-6-250). Afterwards, wells were washed and incubated with Streptavidin-
492 ALP (Mabtech, Cat. 3310-10) for 1 hour. Wells were then washed again and spots were

493 developed with filtered substrate solution BCIP/ NBT-plus (Mabtech, Cat. 3650-10). When
494 distinct spots were visible, the plate was washed and dried overnight. Plates were acquired
495 with an ELISpot reader (AID classic, AID GmbH) and spots were automatically counted using
496 AID ELISpot 8.0 software (AID GmbH).
497 TNFα ELISA was performed with the supernatant from T cell and LCL co-culture as described
498 above using the human TNFα ELISA^{BASIC} kit (Mabtech, Cat. 3512-1H-6), following
499 manufacturer's instructions. Plates were acquired using an ELISA reader (infinite M200Pro,
500 Tecan) and analyzed with the i-control 2.0 software (Tecan).
501
502 **Immunohistochemistry**
503 Tumors were fixed in 4% paraformaldehyde and embedded in paraffin. Sample embedding,
504 preparation and staining was performed by the Pathology department of the University Hospital
505 Basel. Slides were acquired on an automated slide scanning brightfield microscope (Vectra 3,
506 Akoya Biosciences) and quantified using InForm software (Akoya Biosciences).
507
508 **Bulk RNAseq and TCR profiling**
509 RNA was extracted from 5 x 10^6 T cells using the RNeasy® Mini Kit (Qiagen, Cat. 74106). RNA
510 extraction was performed following the instructions from the "Purification of Total RNA from
511 Animal Cells Using Spin Technology" protocol given in the RNeasy® Mini Handbook, including
512 homogenization with QIAshredders (Qiagen, Cat. 79654) and on-column DNA digestion with
513 the RNase-free DNase Set (Qiagen, Cat. 79254). All further steps were performed by the
514 Functional Genomics Center Zurich (FGCZ). The quality of the isolated RNA was determined
515 with a Qubit® (1.0) Fluorometer (Life Technologies, California, USA) and a Bioanalyzer 2100
516 (Agilent, Waldbronn, Germany). Only those samples with a 260 nm/280 nm ratio between 1.8–
517 2.1 and a 28S/18S ratio within 1.5–2 were further processed. The TruSeq RNA Sample Prep
518 Kit v2 (Illumina, Inc, California, USA) was used in the succeeding steps. Briefly, total RNA
519 samples (600 ng) were poly A enriched and then reverse-transcribed into double-stranded
520 cDNA. The cDNA samples were fragmented, end-repaired and polyadenylated before ligation
521 of TruSeq adapters containing the index for multiplexing fragments containing TruSeq adapters

522 on both ends were selectively enriched with PCR. The quality and quantity of the enriched
523 libraries were validated using Qubit® (1.0) Fluorometer and the Caliper GX LabChip® GX
524 (Caliper Life Sciences, Inc., USA). The product is a smear with an average fragment size of
525 approximately 260 bp. The libraries were normalized to 10nM in Tris-Cl 10 mM, pH8.5 with
526 0.1% Tween 20. After library quantification, libraries were prepared for loading accordingly to
527 the NovaSeq workflow with the NovaSeq6000 Reagent Kit (Illumina, Catalog
528 No. 20012865). Cluster generation and sequencing were performed on a NovaSeq6000
529 System with a run configuration of single end 100bp. RNA-seq data analysis consisted of the
530 following steps: The raw reads were first cleaned by removing adapter sequences, trimming
531 low quality ends, and filtering reads with low quality (phred quality <20) using Fastp (Version
532 0.20)[49]. Sequence pseudo alignment of the resulting high-quality reads to the human reference
533 genome (build GRCh38.p13 and GENCODE gene models release 37) and quantification of
534 gene level expression was carried out using Kallisto (Version 0.46.1)[50]. Differential expression
535 was computed using the generalized linear model implemented in the Bioconductor package
536 DESeq2 (R version: 4.2.2, DESeq2 version: 1.38.1)[51]. Genes showing altered expression with
537 adjusted (Benjamini and Hochberg method) p-value < 0.05 were considered differentially
538 expressed. For the TCR analysis the read alignment to the Human genome was performed
539 with STAR (v2.7.10b)[52]. TCR sequences (CDR3 of TRA, TRB, TRG and TRD) were
540 reconstructed from bulk RNAseq data using TRUST4 (v1.0.10)[53]. Out-of-frame sequences
541 were excluded from the analysis. TCR repertoire analysis was performed using the R package
542 Immunarch[54].
543
544 **Statistics**
545 Statistical analysis was performed using Prism 10 Software (GraphPad Software, Inc). Figure
546 legends indicate which statistical test was performed.
547
548 **Study approval**
549 Animal experiments were conducted according to licenses approved by the veterinary office of
550 the canton of Zurich, Switzerland (ZH049/20 and ZH067/2023).

BioRender

Schematics were generated with a licensed version of BioRender.com.

Author contributions

J.M. and O.C. conceived, designed, and evaluated the experiments. J.M. performed the analysis. M.K. and L.E. assisted with the in vivo experiments. L.O. provided bioinformatic analysis of transcriptomic data. O.C. supervised and C.M. cosupervised this work. J.M. and O.C. wrote the manuscript. All authors approved the manuscript.

Declaration of Interests

The authors declare that they have no competing interests.

Acknowledgments

This research was supported by Swiss Cancer Research foundation (KFS-5292-02-2021 to O.C.).

Data Sharing

Supplemental data are provided with this paper. All data are also available from the corresponding author upon reasonable request.

References

1. Simoni, Y. *et al.* Bystander CD8+ T cells are abundant and phenotypically distinct in human tumour infiltrates. *Nature* **557**, 575–579 (2018).
2. Scheper, W. *et al.* Low and variable tumor reactivity of the intratumoral TCR repertoire in human cancers. *Nat Med* **25**, 89–94 (2019).
3. Lan, X., Zebley, C. C. & Youngblood, B. Cellular and molecular waypoints along the path of T cell exhaustion. *Sci Immunol* **8**, eadg3868 (2023).
4. Lowery, F. J. *et al.* Molecular signatures of antitumor neoantigen-reactive T cells from metastatic human cancers. *Science* **375**, 877–884 (2022).
5. Oliveira, G. & Wu, C. J. Dynamics and specificities of T cells in cancer immunotherapy. *Nat Rev Cancer* **23**, 295–316 (2023).
6. Korman, A. J., Garrett-Thomson, S. C. & Lonberg, N. The foundations of immune checkpoint blockade and the ipilimumab approval decennial. *Nat Rev Drug Discov* **21**, 509–528 (2022).
7. Ribas, A. & Wolchok, J. D. Cancer immunotherapy using checkpoint blockade. *Science* **359**, 1350–1355 (2018).
8. Powles, T. *et al.* Atezolizumab with enzalutamide versus enzalutamide alone in metastatic castration-resistant prostate cancer: a randomized phase 3 trial. *Nat Med* **28**, 144–153 (2022).
9. Guan, X. *et al.* Androgen receptor activity in T cells limits checkpoint blockade efficacy. *Nature* **606**, 791–796 (2022).
10. Palmer, A. C., Izar, B., Hwangbo, H. & Sorger, P. K. Predictable Clinical Benefits without Evidence of Synergy in Trials of Combination Therapies with Immune-Checkpoint Inhibitors. *Clin Cancer Res* **28**, 368–377 (2022).
11. Zong, W. *et al.* Transcriptomic congruence analysis for evaluating model organisms. *Proc Natl Acad Sci U S A* **120**, e2202584120 (2023).
12. Gilbertson, S. E. *et al.* Topologically associating domains are disrupted by evolutionary genome rearrangements forming species-specific enhancer connections in mice and humans. *Cell Rep* **39**, 110769 (2022).

13. Medetgul-Ernar, K. & Davis, M. M. Standing on the shoulders of mice. *Immunity* **55**, 1343–1353 (2022).
14. Dong, M. B. *et al.* Systematic Immunotherapy Target Discovery Using Genome-Scale In Vivo CRISPR Screens in CD8 T Cells. *Cell* **178**, 1189-1204.e23 (2019).
15. Chen, Z. *et al.* In vivo CD8+ T cell CRISPR screening reveals control by Fli1 in infection and cancer. *Cell* **184**, 1262-1280.e22 (2021).
16. Puig-Saus, C. *et al.* Neoantigen-targeted CD8+ T cell responses with PD-1 blockade therapy. *Nature* **615**, 697–704 (2023).
17. De La Rochere, P. *et al.* Humanized Mice for the Study of Immuno-Oncology. *Trends Immunol* **39**, 748–763 (2018).
18. Hiwarkar, P. *et al.* Cord blood T cells mediate enhanced antitumor effects compared with adult peripheral blood T cells. *Blood* **126**, 2882–2891 (2015).
19. Baazim, H., Antonio-Herrera, L. & Bergthaler, A. The interplay of immunology and cachexia in infection and cancer. *Nat Rev Immunol* **22**, 309–321 (2022).
20. Utzschneider, D. T. *et al.* T Cell Factor 1-Expressing Memory-like CD8(+) T Cells Sustain the Immune Response to Chronic Viral Infections. *Immunity* **45**, 415–427 (2016).
21. van der Leun, A. M., Thommen, D. S. & Schumacher, T. N. CD8+ T cell states in human cancer: insights from single-cell analysis. *Nat Rev Cancer* **20**, 218–232 (2020).
22. Naulaerts, S. *et al.* Multiomics and spatial mapping characterizes human CD8+ T cell states in cancer. *Sci Transl Med* **15**, eadd1016 (2023).
23. Wolfl, M. *et al.* Activation-induced expression of CD137 permits detection, isolation, and expansion of the full repertoire of CD8+ T cells responding to antigen without requiring knowledge of epitope specificities. *Blood* **110**, 201–210 (2007).
24. Ye, Q. *et al.* CD137 accurately identifies and enriches for naturally occurring tumor-reactive T cells in tumor. *Clin Cancer Res* **20**, 44–55 (2014).
25. Parkhurst, M. *et al.* Isolation of T-Cell Receptors Specifically Reactive with Mutated Tumor-Associated Antigens from Tumor-Infiltrating Lymphocytes Based on CD137 Expression. *Clin Cancer Res* **23**, 2491–2505 (2017).

26. Gros, A. *et al.* PD-1 identifies the patient-specific CD8^{+} tumor-reactive repertoire infiltrating human tumors. *J Clin Invest* **124**, 2246–2259 (2014).
27. Thommen, D. S. *et al.* A transcriptionally and functionally distinct PD-1+ CD8+ T cell pool with predictive potential in non-small-cell lung cancer treated with PD-1 blockade. *Nat Med* **24**, 994–1004 (2018).
28. Gros, A. *et al.* Recognition of human gastrointestinal cancer neoantigens by circulating PD-1+ lymphocytes. *J Clin Invest* **129**, 4992–5004 (2019).
29. Duhen, T. *et al.* Co-expression of CD39 and CD103 identifies tumor-reactive CD8 T cells in human solid tumors. *Nat Commun* **9**, 2724 (2018).
30. Yeong, J. *et al.* Intratumoral CD39+CD8+ T Cells Predict Response to Programmed Cell Death Protein-1 or Programmed Death Ligand-1 Blockade in Patients With NSCLC. *J Thorac Oncol* **16**, 1349–1358 (2021).
31. Lee, Y. J. *et al.* CD39+ tissue-resident memory CD8+ T cells with a clonal overlap across compartments mediate antitumor immunity in breast cancer. *Sci Immunol* **7**, eabn8390 (2022).
32. Palomero, J. *et al.* Biomarkers of tumor-reactive CD4+ and CD8+ TILs associate with improved prognosis in endometrial cancer. *J Immunother Cancer* **10**, e005443 (2022).
33. Chow, A. *et al.* The ectonucleotidase CD39 identifies tumor-reactive CD8+ T cells predictive of immune checkpoint blockade efficacy in human lung cancer. *Immunity* **56**, 93-106.e6 (2023).
34. Buggert, M., Price, D. A., Mackay, L. K. & Betts, M. R. Human circulating and tissue-resident memory CD8+ T cells. *Nat Immunol* **24**, 1076–1086 (2023).
35. Sekine, T. *et al.* TOX is expressed by exhausted and polyfunctional human effector memory CD8+ T cells. *Sci Immunol* **5**, eaba7918 (2020).
36. Brenchley, J. M. *et al.* Expression of CD57 defines replicative senescence and antigen-induced apoptotic death of CD8+ T cells. *Blood* **101**, 2711–2720 (2003).
37. Llaó-Cid, L. *et al.* EOMES is essential for antitumor activity of CD8+ T cells in chronic lymphocytic leukemia. *Leukemia* **35**, 3152–3162 (2021).

38. Amaria, R. N. *et al.* Neoadjuvant relatlimab and nivolumab in resectable melanoma. *Nature* **611**, 155–160 (2022).
39. Guo, X. *et al.* Global characterization of T cells in non-small-cell lung cancer by single-cell sequencing. *Nat Med* **24**, 978–985 (2018).
40. Caushi, J. X. *et al.* Transcriptional programs of neoantigen-specific TIL in anti-PD-1-treated lung cancers. *Nature* **596**, 126–132 (2021).
41. Oliveira, G. *et al.* Phenotype, specificity and avidity of antitumour CD8+ T cells in melanoma. *Nature* **596**, 119–125 (2021).
42. Rohaan, M. W. *et al.* Tumor-Infiltrating Lymphocyte Therapy or Ipilimumab in Advanced Melanoma. *N Engl J Med* **387**, 2113–2125 (2022).
43. Koppensteiner, L. *et al.* Location of CD39+ T cell subpopulations within tumors predict differential outcomes in non-small cell lung cancer. *J Immunother Cancer* **11**, e006770 (2023).
44. Oliveira, G. *et al.* Preexisting tumor-resident T cells with cytotoxic potential associate with response to neoadjuvant anti-PD-1 in head and neck cancer. *Sci Immunol* **8**, eadf4968 (2023).
45. Krishna, S. *et al.* Stem-like CD8 T cells mediate response of adoptive cell immunotherapy against human cancer. *Science* **370**, 1328–1334 (2020).
46. Hanada, K.-I. *et al.* A phenotypic signature that identifies neoantigen-reactive T cells in fresh human lung cancers. *Cancer Cell* **40**, 479-493.e6 (2022).
47. Mestas, J. & Hughes, C. C. W. Of mice and not men: differences between mouse and human immunology. *J Immunol* **172**, 2731–2738 (2004).
48. Chijioke, O. *et al.* Human natural killer cells prevent infectious mononucleosis features by targeting lytic Epstein-Barr virus infection. *Cell Rep* **5**, 1489–1498 (2013).
49. Chen, S., Zhou, Y., Chen, Y. & Gu, J. fastp: an ultra-fast all-in-one FASTQ preprocessor. *Bioinformatics* **34**, i884–i890 (2018).
50. Bray, N. L., Pimentel, H., Melsted, P. & Pachter, L. Near-optimal probabilistic RNA-seq quantification. *Nat Biotechnol* **34**, 525–527 (2016).

51. Love, M. I., Huber, W. & Anders, S. Moderated estimation of fold change and dispersion for RNA-seq data with DESeq2. *Genome Biol* **15**, 550 (2014).
52. Dobin, A. *et al.* STAR: ultrafast universal RNA-seq aligner. *Bioinformatics* **29**, 15–21 (2013).
53. Song, L. *et al.* TRUST4: immune repertoire reconstruction from bulk and single-cell RNA-seq data. *Nat Methods* **18**, 627–630 (2021).
54. Team, I. immunarch: an R package for painless bioinformatics analysis of T-cell and B-cell immune repertoires. *Zenodo* **10**, 5281 (2019).

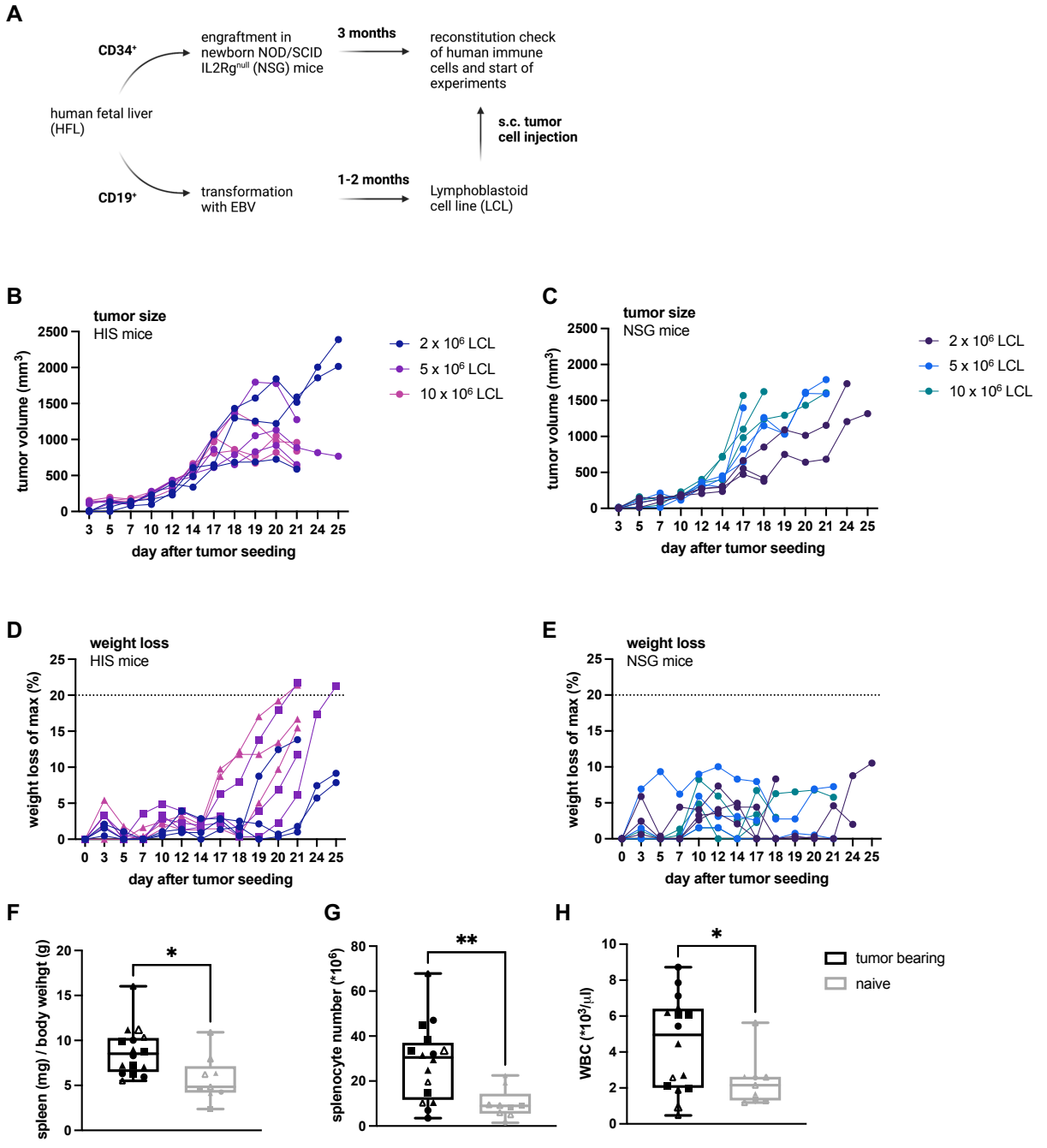

Figure 1: LCL tumor growth kinetics and weight loss in autologous HIS mice and NSG mice. LCL tumors were injected subcutaneously into the flank of mice and tumor size was assessed by calipering. **A**, schematic of generation of HIS mice and autologous tumor cells and subsequent injection in HIS mice. **B**, tumor volume in HIS mice after implantation of the indicated number of LCLs. **C,** Tumor volume in NSG mice after implantation of the indicated number of LCLs. (D, E) Relative weight loss calculated based on the maximum weight during the experiment after tumor cell implantation of the indicated number of LCLs in HIS (**D**) or NSG (**E**) mice. **F**, ratio of spleen weight (mg) to body weight (g), **G**, total splenocyte number and **H**, white blood cell count in HIS mice injected with 5 x 10^6 autologous LCL tumor cells or non-

589 tumor bearing HIS mice (naïve) sacrificed 15-20 days after tumor implantation. B-E, n=3 per
590 tumor cell number, F-H, n(tumor-bearing)=16, n(naïve)=9 from 4 individual experiments,
591 marked by individual symbols. Unpaired t-test, data shown as box and whiskers with the box
592 from the 25-75 percentile and the median is shown as a line within the box; whiskers are shown
593 from minimum to maximum data point.

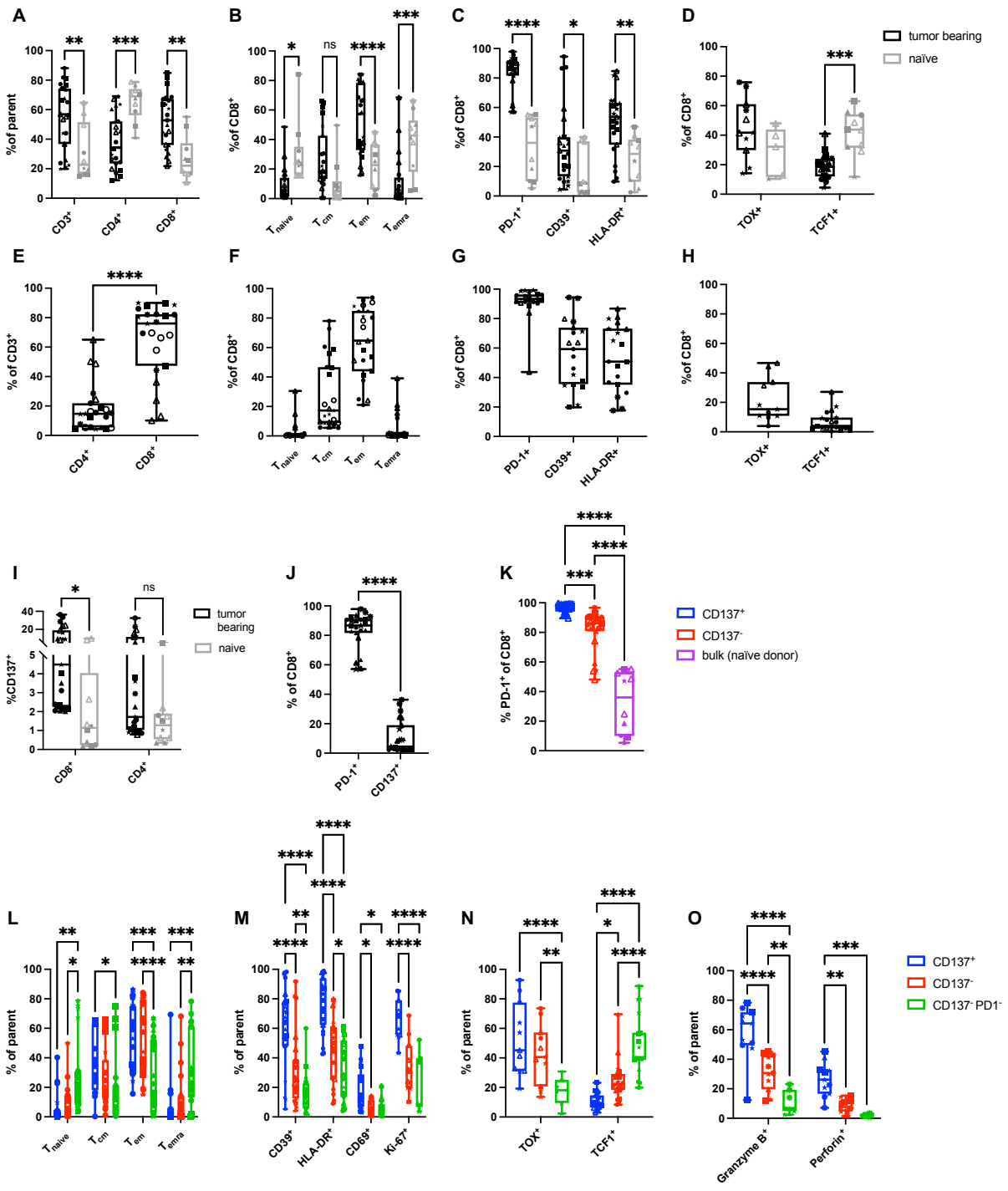

Figure 2: T cell response in tumor-bearing HIS mice. Splenocytes (A-D) and tumor-infiltrating lymphocytes (TIL) (E-H) were isolated from HIS mice 16-18 days after tumor implantation and analyzed by flow cytometry. **A,** frequency of splenic T cells in tumor-bearing or naïve HIS mice; parent population refers to frequency (%) of $CD3^+$ T cells within human $CD45^+$ cells and $CD4^+$ and $CD8^+$ T cells within $CD3^+$ T cells. **B**, $CD8^+$ T cell differentiation defined as $T_{naïve}$ ($CD45RA^+CD62L^+$), T_{CM} ($CD45RA^-CD62L^+$), T_{EM} ($CD45RA^-CD62L^-$), T_{EMRA} ($CD45RA^+CD62L^-$) in tumor-bearing or naïve HIS mice. **C-D**, expression of indicated markers on $CD8^+$ T cells from spleen of tumor-bearing or naïve HIS mice. **E,** frequency of $CD4^+$ and

602 $CD8^+$ T cells within TILs, gated on total $CD3^+$ T cells. **F,** $CD8^+$ T cell differentiation within TILs.
603 **G-H,** expression of indicated markers on $CD8^+$ T cells within TILs. **I,** expression of CD137 on
604 splenic $CD8^+$ and $CD4^+$ T cells of tumor-bearing or naïve HIS mice. **J,** expression of PD-1 and
605 CD137 on splenic $CD8^+$ T cells of tumor-bearing mice. **K**, expression of PD-1 on splenic $CD8^+$
606 T cells based on CD137 in tumor-bearing HIS mice or bulk $CD8^+$ T cells from naïve HIS mice.
607 **L,** $CD8^+$ T cell differentiation in spleen of tumor-bearing HIS mice. **M-O**, expression of indicated
608 markers on splenocyte-derived $CD8^+$ T cell populations based on expression of CD137 and
609 PD-1. Data are pooled from at least 3 independent experiments, n=10-23 mice per group. For
610 each experiment, a different HPC donor was used for HIS mouse reconstitution and generation
611 of autologous tumor. Significance by paired t-test, one-way ANOVA or 2way ANOVA, as
612 appropriate. Data from individual experiments are indicated by different symbols.

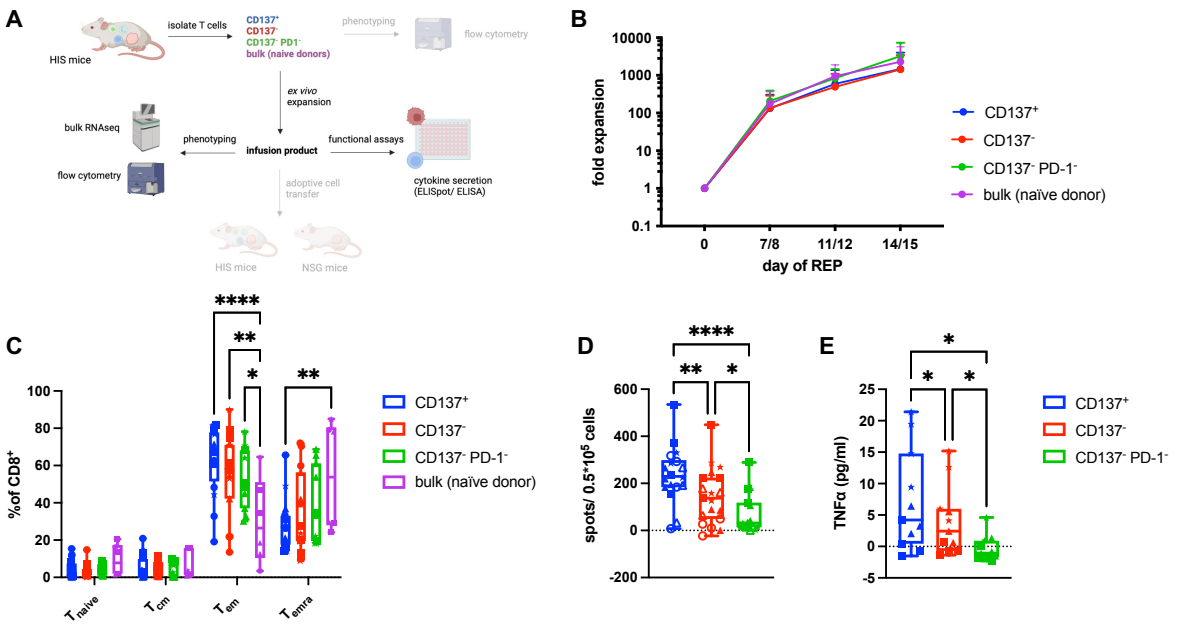

Figure 3: Exhausted-like human CD8$^+$ T cells derived from tumor-bearing HIS mice can be expanded *ex vivo* and exhibit superior tumor-specific cytokine production. A, schematic of generation, expansion and characterization of T cells from HIS mice bearing autologous LCL tumors. **B**, fold expansion of FACS sorted splenic CD8$^+$ T cells from tumor-bearing HIS mice (CD137$^+$, CD137$^-$ and CD137$^-$PD1$^-$) or naïve HIS mice (bulk). **C**, CD8$^+$ T cell differentiation after *ex vivo* expansion defined as $T_{naïve}$ (CD45RA$^+$CD62L$^+$), T_{CM} (CD45RA$^-$CD62L$^+$), T_{EM} (CD45RA$^-$CD62L$^-$), T_{EMRA} (CD45RA$^+$CD62L$^-$). **D**, IFN-γ ELISpot of expanded T cells in 5:1 (E:T) co-culture with autologous LCL tumor cells for 24 hours. Spot count is normalized to the spots produced by expanded CD8$^+$ bulk T cells from naïve HIS mice. **E**, TNFα ELISA of supernatant of expanded T cells in co-culture (5:1, E:T) with autologous LCL tumor cells for 24 hours. TNFα concentration is normalized to the TNFα secretion from expanded CD8$^+$ bulk T cells derived from naïve mice. Data are pooled from at least 3 independent experiments, n=6-19 mice per group. For each experiment, a different HPC donor was used for HIS mouse reconstitution and generation of autologous tumor. Significance by mixed-effects analysis (paired), RM one-way ANOVA or 2way ANOVA, as appropriate. Data from individual experiments are indicated by different symbols.

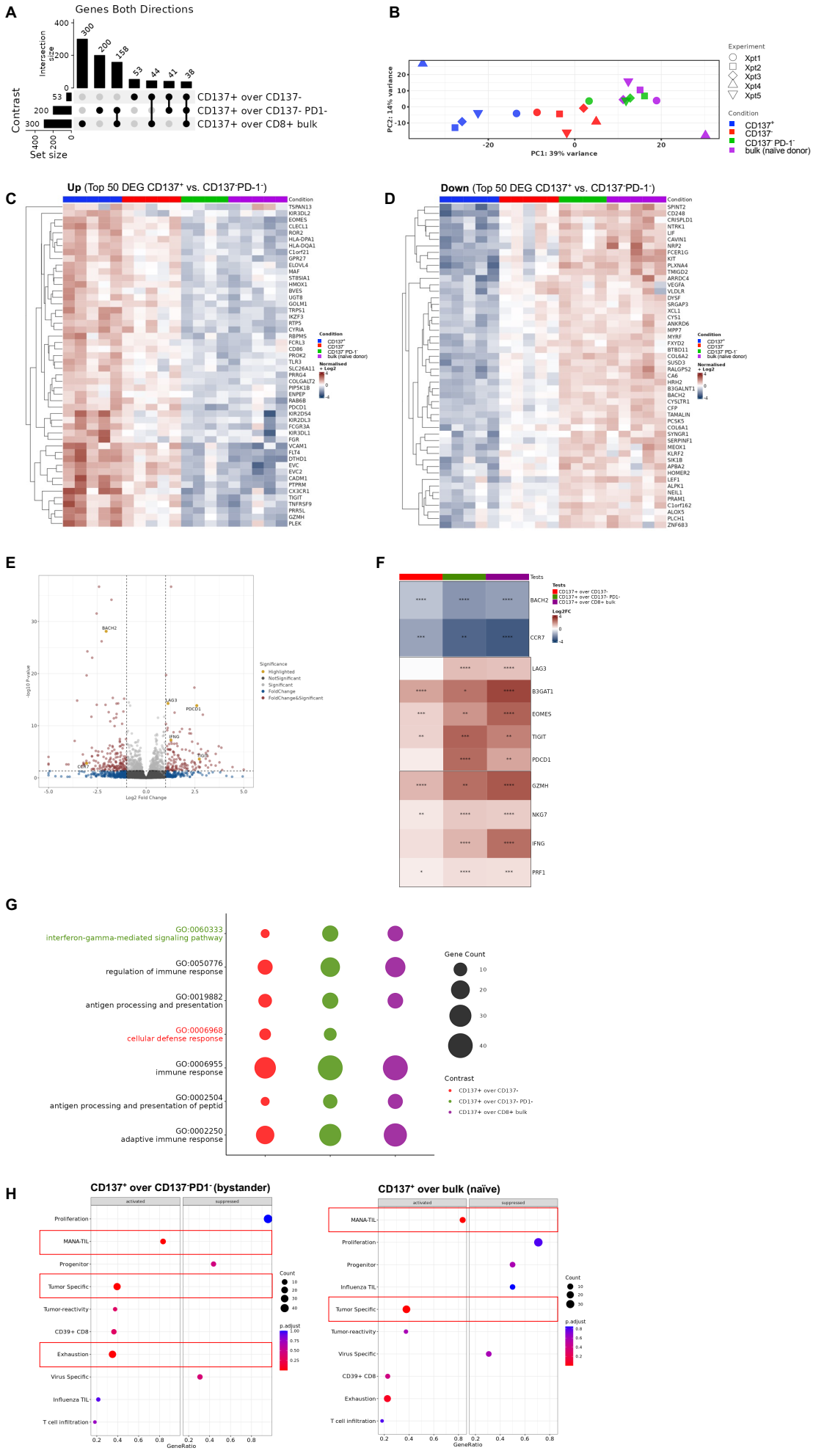
A
Genes Both Directions
Intersection size
Contrast
Set size
CD137+ over CD137-
CD137+ over CD137- PD1-
CD137+ over CD8+ bulk
B
Experiment
Xpt1
Xpt2
Xpt3
Xpt4
Xpt5
Condition
CD137+
CD137-
CD137- PD-1-
bulk (naïve donor)
PC2: 14% variance
PC1: 39% variance
C
Up (Top 50 DEG CD137+ vs. CD137-PD-1-)
D
Down (Top 50 DEG CD137+ vs. CD137-PD-1-)
E
Significance
Highlighted
NotSignificant
Significant
FoldChange
FoldChange&Significant
Log2 Fold Change
F
Tests
CD137+ over CD137-
CD137+ over CD137- PD1-
CD137+ over CD8+ bulk
Log2FC
BACH2
CCR7
LAG3
B3GAT1
EOMES
TIGIT
PDCD1
GZMH
NKG7
IFNG
PRF1
G
GO:0060333
interferon-gamma-mediated signaling pathway
GO:0050776
regulation of immune response
GO:0019882
antigen processing and presentation
GO:0006968
cellular defense response
GO:0006955
immune response
GO:0002504
antigen processing and presentation of peptid
GO:0002250
adaptive immune response
Gene Count
Contrast
CD137+ over CD137-
CD137+ over CD137- PD1-
CD137+ over CD8+ bulk
H
CD137+ over CD137-PD1- (bystander)
CD137+ over bulk (naïve)
activated
suppressed
Proliferation
MANA-TIL
Progenitor
Tumor Specific
Tumor-reactivity
CD39+ CD8
Exhaustion
Virus Specific
Influenza TIL
T cell infiltration
Count
p.adjust
GeneRatio

629 **Figure 4: Transcriptomic profiling of tumor-reactive CD137$^+$CD8$^+$ T cells**

630 Transcriptome analysis and pathway analysis of expanded CD8$^+$ T cells from tumor-bearing
631 HIS mice (CD137$^+$, CD137$^-$ and CD137$^-$PD1$^-$) or naïve HIS mice (bulk). **A,** Upset plot (intersect)
632 showing number of differentially expressed genes between groups in bulk RNAseq. p(FDR) <
633 0.05, log2 FC > 1.5. **B**, PCA plot of RNAseq showing PC1 and PC2. **C,** Top 50 upregulated
634 and **D,** downregulated genes of T cell subsets based on the DEG between CD137$^+$ vs. CD137$^-$
635 PD1$^-$ CD8$^+$ T cells. p(FDR) < 0.05, log2 FC > 1.5. **E,** Volcano plot showing DEG between
636 CD137$^+$ and CD137$^-$PD1$^-$CD8$^+$ T cells with genes of interest highlighted in yellow. **F**, differential
637 expression of genes of interest between groups. **G**, Overrepresentation analysis (ORA) of
638 upregulated pathways in CD137$^+$CD8$^+$ T cells. **H**, Gene set enrichment analysis (GSEA) of
639 signatures described on the y-axis. Gene ratio (# genes related to GO term / total number of
640 sig genes) is displayed on the x-axis. Signatures with an adjusted p-value <0.05 are highlighted
641 with a red box. Shown are data from 5 individual experiments, each experiment with different
642 human HPC donor for reconstitution of HIS mice and autologous tumor.

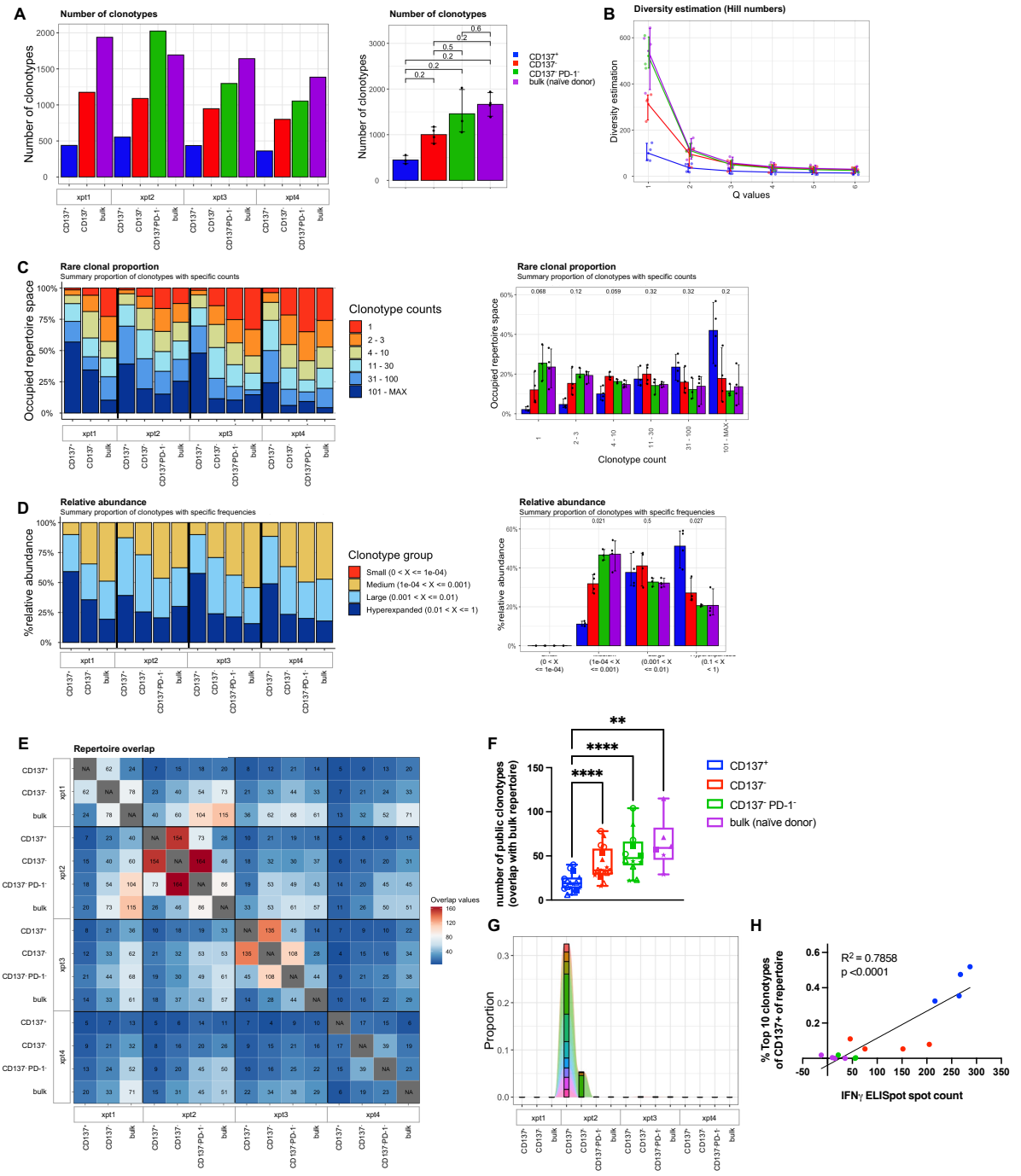

Figure 5: TCR profiling of tumor-reactive CD137$^+$CD8$^+$ T cells. A, total number of individual clonotypes found per population. Left: data from individual experiments, right: pooled data for group analysis. Wilcoxon test. **B,** TCR (CDR3 of *TRA*, *TRB*, *TRG* and *TRD*) sequence sample diversity estimation using Hill numbers method, with Q=1 describing the Shannon diversity. **C,** rare clonal proportion showing the occupied repertoire space by clonotypes with defined counts (1, 2-3, 4-10, etc.). Left: data from individual experiments, right: pooled data for group analysis. Wilcoxon test. **D,** relative abundance of clonotypes with defined frequencies (size). Left: data from individual experiments, right: pooled data for group analysis. Wilcoxon test. **E,**

651 repertoire overlap analysis cross-comparing every population from every experiment (each
652 with different donor). **F**, repertoire overlap comparing the repertoire of bulk $CD8^+$ T cells from
653 naïve HIS mice to the populations from tumor-bearing HIS mice from individual experiments
654 (each with different donor; data from individual experiments are indicated by different symbols).
655 Mixed effects analysis with Tukey's multiple comparisons test. **G**, tracking of clonotypes over
656 populations. The top 10 most abundant clonotypes of the TCR repertoire of $CD137^+CD8^+$ T
657 cells from one representative experiment are shown. **H**, proportion of the top 10 most abundant
658 clonotypes (from repertoires of $CD137^+CD8^+$ T cells) in the repertoire of all populations,
659 correlated with the spot count of IFN-γ ELISpot. Shown are data from 4 individual experiments,
660 each experiment with different human HPC donor for reconstitution of HIS mice and autologous
661 tumor.

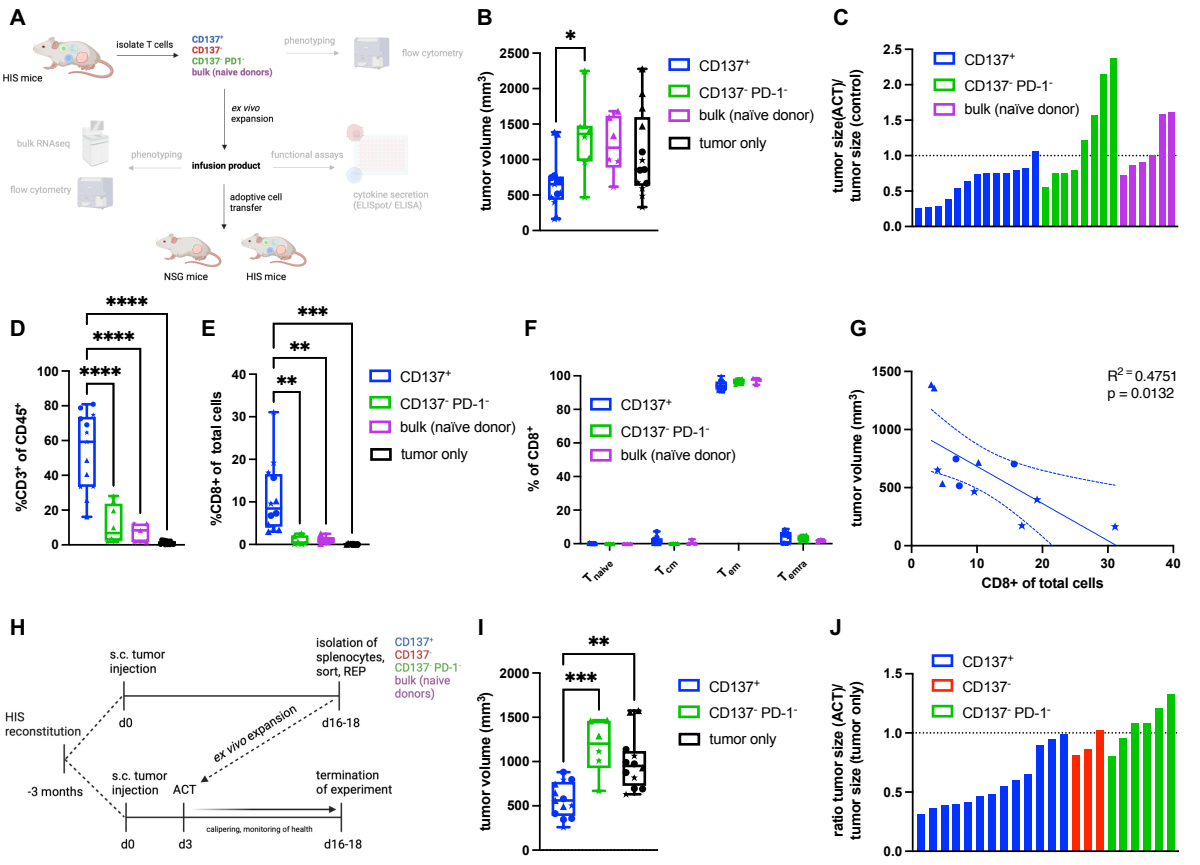

Figure 6: CD137$^+$CD8$^+$ T cells from tumor-bearing HIS mice show superior anticancer activity in NSG and HIS recipients bearing autologous tumors. A, schematic of generation of tumor-reactive T cells and subsequent ACT. NSG mice were injected with 2 x 10^6 LCL s.c. in the flank and after three days, 10 x 10^6 *ex vivo* expanded T cells were adoptively transferred intravenously. Transferred T cells and LCL tumors were autologous to each other. **B**, tumor volume on the day of sacrifice in NSG recipient mice after ACT of the indicated cell populations. **C,** waterfall plot of tumor size in NSG recipient mice of ACT on the day of sacrifice relative to the tumor volume of control mice (no ACT). Bars depict individual mice. **D**, frequency of CD3$^+$ T cells (% of human CD45$^+$ cells) in TIL from NSG mice after ACT of the indicated cell populations, measured by flow cytometry. **E**, frequency of CD8$^+$ T cells (% of total cells) in tumors of NSG mice after ACT of the indicated cell populations, measured by immunohistochemistry. **F**, differentiation of CD8$^+$ T cells in TIL of NSG mice after ACT of the indicated cell populations defined as $T_{naïve}$ (CD45RA$^+$CD62L$^+$), T_{CM} (CD45RA$^-$CD62L$^+$), T_{EM} (CD45RA$^-$CD62L$^-$) and T_{EMRA} (CD45RA$^+$CD62L$^-$). **G,** correlation between tumor volume and infiltration of CD8$^+$ T cells (measured by IHC) in tumors of NSG mice after adoptive transfer of CD137$^+$CD8$^+$ T cells. **H**, schematic of ACT. CD137$^+$CD8$^+$ T cells, CD137$^-$CD8$^+$ T cells and

678 CD137$^-$ PD-1$^-$CD8$^+$ T cells were isolated from spleen of tumor-bearing HIS mice or bulk CD8$^+$
679 T cells from spleen of naïve HIS mice and expanded *ex vivo*. Recipient HIS mice were injected
680 with 2 x 10^6 LCL s.c. in the flank and after three days, *ex vivo* expanded T cells were adoptively
681 transferred intravenously. Tumor-bearing HIS recipient mice received 2 x 10^6 T cells without
682 prior conditioning/lymphodepletion. Donor and recipient HIS mice as well as LCL were
683 autologous to each other. **I,** tumor volume on the day of sacrifice in HIS recipient mice after
684 ACT of the indicated cell populations. **J,** waterfall plot of tumor size on the day of sacrifice of
685 HIS mice receiving ACT relative to the tumor volume of control HIS mice (no ACT). Bars depict
686 individual mice. B-G: Data are pooled from 2-3 independent experiments, n=6-13 per group. I,
687 data are pooled from 2-3 independent experiments (n=6-13 per group); J, data are from 1-3
688 independent experiments (n=3-13 per group). For each experiment, a with different HPC donor
689 was used for HIS mouse reconstitution and generation of autologous tumor. Significance by
690 one-way ANOVA. Data from individual experiments are indicated by different symbols.